



Deposited via The University of Sheffield.

White Rose Research Online URL for this paper:

<https://eprints.whiterose.ac.uk/id/eprint/108114/>

Version: Accepted Version

Article:

Brown, S., Peristeras, L.D., Martynov, S. et al. (2016) Thermodynamic interpolation for the simulation of two-phase flow of non-ideal mixtures. *Computers & Chemical Engineering*, 95. C. pp. 49-57. ISSN: 0098-1354

<https://doi.org/10.1016/j.compchemeng.2016.09.005>

Article available under the terms of the CC-BY-NC-ND licence
(<https://creativecommons.org/licenses/by-nc-nd/4.0/>)

Reuse

Items deposited in White Rose Research Online are protected by copyright, with all rights reserved unless indicated otherwise. They may be downloaded and/or printed for private study, or other acts as permitted by national copyright laws. The publisher or other rights holders may allow further reproduction and re-use of the full text version. This is indicated by the licence information on the White Rose Research Online record for the item.

Takedown

If you consider content in White Rose Research Online to be in breach of UK law, please notify us by emailing eprints@whiterose.ac.uk including the URL of the record and the reason for the withdrawal request.

Thermodynamic interpolation for the simulation of two-phase flow of complex mixtures

S. Brown^{1,2}, L. D. Peristeras³, S. Martynov², R. T. J. Porter², H. Mahgerefteh^{2,*}, Ilias K. Nikolaidis³, Georgios C. Boulougouris^{3,4}, Dimitrios M. Tsangaris³ and Ioannis G. Economou^{3,5}

*corresponding author h.mahgerefteh@ucl.ac.uk

¹*Current address: Department of Chemical and Biological Engineering, The University of Sheffield, Mappin Street S1 3JD, UK*

²*Department of Chemical Engineering, University College of London, London WC1E7JE, UK*

³*National Center for Scientific Research "Demokritos", Institute of Nanoscience and Nanotechnology, Molecular Thermodynamics and Modelling of Materials Laboratory, Agia Paraskevi, Attikis GR-153 10, Greece*

⁴*Department of Molecular Biology and Genetics, Democritus University, 68100, Alexandroupolis, Greece*

⁵*Texas A&M University at Qatar, Chemical Engineering Program, 23874 Doha, Qatar*

Abstract

This paper describes the development and application of a technique for the rapid interpolation of thermodynamic properties of mixtures for the purposes of simulating two-phase flow. The technique is based on adaptive inverse interpolation and can be applied to any Equation of State and multicomponent mixture. Following analysis of its accuracy, the method is coupled with a two-phase flow model, based on the homogeneous equilibrium mixture assumption, and applied to the simulation of flows of carbon dioxide (CO₂) rich mixtures. This coupled flow model is used to simulate the experimental decompression of binary and quinary mixtures. It is found that the predictions are in good agreement with the experimental data and that the interpolation approach provides a flexible, robust means of obtaining thermodynamic properties for use in flow models.

Keywords: Carbon dioxide transport, Two-phase flow, Equations of state, Pipeline safety

1. Introduction

The modelling of compressible two-phase or flashing flows is common place in a wide range of areas in engineering. For example, cavitation in automotive fuel injection systems (Martynov et al., 2006), flash boiling of water during loss-of-coolant accidents in nuclear reactors (Blinkov et al., 1993) and liquid boiling and expansion in refrigeration systems and heat pumps (Simões-Moreira and Bullard, 2003). Whilst various approaches are available to model the dynamics of two-phase flow, the accuracy of simulations for flashing two-phase flows to a large extent depends on the accuracy of

37 the physical properties data in use. This particularly applies to multi-component mixtures, which are
38 commonly found as working fluids in the above systems.

39 In practice, complex mathematical formulas known as Equations of State (EoS), are used to provide
40 the thermodynamic properties for both vapour and liquid phases. As a result, a practical problem
41 arises when pressure explicit EoS are coupled with flow models. In these EoS, the thermodynamic
42 properties are predicted as a function of pressure, temperature and composition while phase
43 equilibria, at a given system pressure and temperature (P-T), is determined using a variety of
44 isothermal 'flash' algorithms (M. Michelsen, 1982; M. L. Michelsen, 1982). This formulation contrasts
45 with the fluid-dynamics models, where the conservation laws governing are naturally posed in terms
46 of density and internal energy (ρ -U). To overcome this problem, one possible solution is to use the
47 so-called isochoric-isoenergetic flash (Castier, 2009; Michelsen, 1999). However, existing isochoric-
48 isoenergetic flash algorithms are neither robust nor computationally efficient in the context of flow
49 simulation because they either rely on an internal iterative loop over the P-T variables (Michelsen,
50 1999; Saha and Carroll, 1997) or on the direct minimisation of total entropy (Castier, 2009;
51 Munkejord and Hammer, 2015).

52 The problem of computational inefficiency is exacerbated by the complexity of modern EoS. For
53 example, for the case of CO₂ and its mixtures, high accuracy is provided by SAFT EoS (Diamantonis
54 and Economou, 2011) or by the "reference" EoS (Span and Wagner, 1996) and both EoS have a large
55 number of relatively complex terms. As a result, application of these EoS to flow simulations not only
56 increases the computational cost, but also the susceptibility to numerical instabilities in the
57 underlying isothermal flash algorithms.

58 This is a particular problem in the simulation of flows associated with Carbon Capture and Storage
59 (CCS), where the CO₂ stream may contain a number of impurities and vary in composition (Porter et
60 al., 2015). Indeed, it is well established that the presence of these impurities has important impacts
61 on many aspects where the modelling of two-phase flow is relevant, including ductile fracture
62 (Mahgerefteh et al., 2012a) and the release rate in the case of loss of containment (Brown et al.,
63 2013).

64 Previous work to address this issue has focused on producing tables of thermodynamic properties
65 from isenthalpic or isentropic flash calculations (Mahgerefteh et al., 2006), which are facilitated by
66 changing the variables with which the flow is resolved, or using isothermal tables for use in the
67 iterative loop (Andresen, 2009). The former of these means that alternative numerical techniques
68 must be applied and that conservation of mass, momentum and energy is not ensured. Dumbser et
69 al. (2013) presented a method of building an interpolating function using adaptive mesh refinement
70 for a single component fluid; however this relied on the ability to calculate isochoric-isoenergetic
71 flashes which cannot be done efficiently for mixtures.

72 In this work a robust technique for efficiently performing isochoric-isoenergetic flashes, for the
73 purposes of two-phase flow calculations, is presented. The technique is based on adaptive inverse
74 interpolation and can be applied independently of the EoS and the specific mixture under
75 consideration. The technique is intended for the application of the complex, computationally heavy
76 EoS that are required for the accurate prediction of the thermodynamic properties and phase
77 equilibria of CO₂ mixtures. This is then coupled with a two-phase flow model based on the
78 homogeneous equilibrium mixture assumption (Brown et al., 2015a; Mahgerefteh et al., 2012b) and
79 applied to the simulation of CCS relevant two-phase flows.

80 This paper is structured as follows: Section 2 firstly presents the fluid flow model applied in this
81 study (Section 2.1) followed by a description of the interpolation technique developed (Section 2.2).
82 The section ends with an overview of the EoS used in this work.

83 Section 3 provides an analysis of the interpolation technique's consistency with the EoS (Section
84 3.1). Next, the method is coupled with the two-phase flow model and a number of tests are
85 performed to establish the robustness and computational efficiency of the method in the presence
86 of rapid transients (Section 3.2). This coupled flow model is then used to predict the decompression
87 of several mixtures and the results are compared against available experimental data (Section 3.3).
88 Conclusions and suggestions for future work are discussed in Section 4.

89 2. Methodology

90 2.1. The Homogeneous Equilibrium Model (HEM) flow model

91 The model applied in this study is based on the assumptions of one-dimensional, unsteady flow and,
92 in the case of two-phase flow, thermodynamic and mechanical equilibrium, i.e. a single temperature,
93 pressure and velocity, between the saturated vapour and liquid phases. In this case the respective
94 continuity, momentum, and energy conservation equations are given by (see for example Zucrow
95 and Hoffman, 1975):

$$\frac{\partial \rho}{\partial t} + \frac{\partial \rho u}{\partial z} = 0 \quad (1)$$

96

$$\frac{\partial \rho u}{\partial t} + \frac{\partial \rho u^2 + P}{\partial z} = -\frac{f_w \rho u^2}{D_p} \quad (2)$$

97

$$\frac{\partial E}{\partial t} + \frac{\partial u(E + P)}{\partial z} = -u \frac{f_w \rho u^2}{D_p}. \quad (3)$$

98 where ρ , u , P are respectively the mixture density, velocity and pressure, which are functions of
99 time, t , and spatial coordinate, z ; D_p and f_w , are the pipeline diameter and Fanning friction factor,
100 calculated using Chen's correlation (Chen, 1979), and E is the total mixture energy defined as:

$$E = \rho \left(e + \frac{1}{2} u^2 \right) \quad (4)$$

101 where e is the mixture specific internal energy:

$$e = x_{eq} e_v + (1 - x_{eq}) e_l \quad (5)$$

102 x_{eq} is the equilibrium vapour quality, and ρ is the mixture density defined as:

103

$$\frac{1}{\rho} = \frac{x_{eq}}{\rho_v} + \frac{(1 - x_{eq})}{\rho_l}. \quad (6)$$

104 In equations (5) and (6) the subscripts v and l refer to the vapour and liquid phases respectively.

105 To solve equations (1) to (3) numerically, a finite volume method is used (Leveque, 2002), where,
 106 following Brown et al. (2015b), the conservative left-hand-side of equations (1) to (3) are solved
 107 using the AUSM+ flux vector splitting scheme (Liou, 2006).

108 2.2. Interpolation technique

109 As described previously, the coupling of the EoS described in Section 2.3 with the flow equations ((1)
 110 to (3)) where the fluid is two-phase is complicated by the fact that the free variables are the density,
 111 ρ , and internal energy, e , with which we must compute the system P and T, while the computation
 112 of the phase equilibria using an EoS (in this case PC-SAFT as described in section 2.3) is most
 113 commonly performed using the P and T of a mixture at a given composition. To overcome this, we
 114 introduce the construction of two interpolant grids, one of which is constructed using the P and T as
 115 free variables, denoted {P, T}, and the other using ρ and e , denoted by $\{\rho, e\}$. These grids provide the
 116 means for rapidly computing the thermodynamic properties and phase equilibria during flow
 117 simulations.

118 The construction begins by defining the bounds of the {P,T} grid using the fluid conditions required
 119 for the simulation (i.e. the intervals $[T_{min}, T_{max}]$ and $[P_{min}, P_{max}]$). Grid points are sampled along
 120 isotherms which are uniformly distributed within the temperature range. Typically, for the pressure
 121 ranges of interest for CO₂ pipeline decompression, the isotherms will intersect the dew and bubble
 122 point and hence pass through the phase envelope. As a result, an interpolant has to be developed
 123 which can resolve the abrupt changes of the fluid properties with pressure and temperature within
 124 the phase coexistence regions, and in particular near the equilibrium lines. In practice this means
 125 that the points selected for building the interpolant cannot be uniformly distributed along the
 126 isotherm, but must be chosen so as to resolve the region around, and within, the phase envelope of
 127 the mixture, which is known *a priori* given the composition of the fluid.

128 In order to address this problem and improve the mapping, we adopt a non-uniform sampling along
 129 each isotherm, resulting in an increased density of points close to the dew and bubble point
 130 pressures (P_d and P_b respectively) and within the phase envelope itself. The set of N points along
 131 each isotherm are selected as follows:

- 132 a. if $P_{max} \leq P_d$ or $P_b \leq P_{min}$, i.e. a permanently single-phase fluid, the points are
 133 uniformly distributed in $[P_{max}, P_{min}]$:

$$P_i = P_{min} + (i - 1) \frac{P_{max} - P_{min}}{N - 1}, \quad i = 1, \dots, N \quad (7)$$

- 134 b. if $P_{min} \leq P_d \leq P_b \leq P_{max}$, i.e. the interval $[P_{min}, P_{max}]$ encompasses the two-phase
 135 region, N_d points are distributed in $[P_{min}, P_d - \Delta]$ to increase the point density close
 136 to the dew point using:

$$P_i = P_{min} + (P_d - \Delta - P_{min}) g\left(\frac{i - 1}{N_d}\right), \quad i = 1, \dots, N_d \quad (8)$$

- 137 N_b points are distributed uniform in $[P_b + \Delta, P_{max}]$ to increase the point density
 138 close to the bubble point using:

$$P_i = (P_b + \Delta - P_{min}) + (P_{max} - P_b - \Delta) g\left(\frac{i - 1}{N_b}\right), \quad i = 1, \dots, N_b \quad (9)$$

139 while the remaining N_{VLE} points are distributed using the mapping function which
 140 increases the points density near the dew and the bubble line:

$$P_i = (P_d - \Delta) + (P_b - P_d + 2\Delta) g\left(\frac{i-1}{N_{VLE}}\right), \quad i = 1, \dots, N_{VLE} \quad (10)$$

141 with:

$$g(x) = \frac{1 + \operatorname{erf}(Ax - B)}{2} \quad (11)$$

142 c. if $P_{min} \leq P_d \leq P_{max} \leq P_b$ or $P_d \leq P_{min} \leq P_b \leq P_{max}$, i.e. the interval $[P_{min}, P_{max}]$ contains
 143 part of the two-phase region a variant of the points distribution described in case b
 144 is applied. For example if $P_{min} \leq P_d \leq P_{max} \leq P_b$, the points are distributed according to
 145 (8) and (10), with the exception that in (10) P_{max} is taken as the upper limit rather
 146 than $P_b + \Delta$.

147 In case b, the most general, the number of points N_{VLE} is taken as 70 % of the total number N , while
 148 N_d and N_b are each taken as 15 % of N . The total number of points, N , as well as the distribution
 149 function parameters Δ , A and B are tuned to optimise grid's quality. In this study A and B were set
 150 equal to 4.4 and 2.2 respectively while the values used for N and Δ are reported in later sections.

151 At each of these points, using the P and T , the other thermodynamic properties are calculated (e.g. e ,
 152 ρ). In other words, at these points we have established the maps $e(P, T)$ and $\rho(P, T)$. Using these same
 153 points we re-interpret the grid to give us the inverse maps $P(e, \rho)$ and $T(e, \rho)$, and hence a $\{\rho, e\}$ grid.

154 In order to increase the accuracy of this new grid across the ranges of densities and internal energies
 155 covered, we redistribute the points along an isotherm map $T(e, \rho)$ crossing the phase envelope. The
 156 corresponding path is expressed as a mono-parametric curve $(e(\lambda), \rho(\lambda))$ with $0.0 \leq \lambda \leq 1.0$.

157 Eventually, the properties of interest along this curve are also expressed as functions of the same
 158 parameter i.e. $T(\lambda)$, $P(\lambda)$. Using appropriate values of λ we resample the path to obtain more
 159 uniformly distributed points along the isotherm while the desired properties at the new point are
 160 calculated by interpolating the corresponding functions using univariate Akima splines (Akima,
 161 1996). Finally, we resample the $\{\rho, e\}$ grid produced for each property of interest by using the
 162 bivariate Akima spline interpolation scheme (Akima, 1996) to improve its uniformity/regularity and
 163 consequently the efficiency of the interpolation.

164 2.3. Equations of State

165 In the present study in order to predict the properties of CO_2 and its mixtures, the Perturbed Chain-
 166 Statistical Associating Fluid Theory (PC-SAFT) EoS presented by Diamantonis et al. (2013a) is applied,
 167 a brief description is given next. The PC-SAFT EoS is expressed as the summation of residual
 168 Helmholtz free energy terms that occur due to different types of intermolecular interactions
 169 between the various components in the system under study. The residual Helmholtz free energy,
 170 A_{res} is equal to the Helmholtz free energy minus the Helmholtz free energy of the ideal gas at given
 171 temperature and density. For a system that consists of associating chains (for example aqueous
 172 mixtures), PC-SAFT can be expressed as:

$$\frac{A^{res}(\rho, T)}{NRT} = \frac{a^{hs}}{RT} + \frac{a^{chain}}{RT} + \frac{a^{disp}}{RT} + \frac{a^{assoc}}{RT}, \quad (12)$$

173 where a is the Helmholtz free energy per mole, R is the universal gas constant and the superscripts
174 “res”, “hs”, “chain”, “disp”, and “assoc” refer to residual, hard sphere, chain (hard chain reference
175 fluid), dispersion, and association, respectively. The mathematical expressions for the individual
176 terms may be found in Diamantonis et al. (2013b). More details on the SAFT EoS and its variants for
177 pure components and their mixtures are given in Kontogeorgis and Folas (2010).

178 3. Results and discussion

179 3.1. Interpolation consistency analysis

180 Prior to its application to flow simulations the consistency of the interpolation method with the
181 underlying thermodynamic model must be assessed. For the subsequent analysis, two mixtures are
182 chosen; a simple binary mixture of CO₂ and nitrogen (N₂) and a more complex quinary mixture of
183 hydrogen (H₂), oxygen (O₂), N₂, methane (CH₄) and CO₂ (Tests 26 and 31 respectively presented by
184 Cosham et al., 2012). The composition of each mixture is shown in Table 1. The construction of the
185 tables used a total of 100 isotherms along which N was taken to be 200, while Δ is set to zero. It
186 should be noted that, due to the extended P and T conditions of the experimental data, and hence
187 lower pressures and temperatures, produced for the binary mixture presented in Section 3.3, it is
188 necessary to produce a table which extends to far lower temperatures. Figures 1 (a) and (b)
189 respectively show the points sampled for the $\{\rho, e\}$ constructed for the binary mixture using a
190 uniform $\{P, T\}$ grid and using the methodology developed above. The $\{P, T\}$ grid developed for this
191 latter is shown in Figure 2. As can clearly be seen in Figure 1 (a) the “uniform sampling strategy”
192 produces in a much sparser weighting of the points through the phase envelope compared to the
193 one achieved in (b) where the re-distribution of the points results in a much greater number of
194 samples between the dew and bubble point lines.

195 In order to quantify the deviations of the predictions obtained from the interpolation grids and the
196 actual values calculated from the underlying EoS, 10,000 random samples are taken in the relevant
197 P-T domain. From these samples, the $e(P, T)$ and $\rho(P, T)$ functions are evaluated using the EoS and the
198 application of the interpolation grids using these values compared with the original point. Table 2
199 presents the percentage average absolute deviations (% AAD) of the predictions obtained from this
200 analysis for both the binary and quinary mixtures. It should be noted that the grid produced
201 from the uniform $\{P, T\}$ sampling failed to provide predictions for all of the points used in this
202 comparison and so is omitted. As may be observed, with the exception of the binary pressure
203 predictions for which a value of 0.44 % was found, the results show an AAD% of less than 0.1%.

204 Figures 3 (a) and (b) show the %AAD contours of the predicted temperature and pressure
205 respectively, for the binary mixture. Figures 4 (a) and (b) shows the same data for the quinary
206 mixture. As can be seen from both Figures 3 and 4 the error observed in the prediction of the
207 pressure is substantially higher in places, reaching up to 10 %, than for the temperature, which is
208 less than 0.5 % throughout; nevertheless, the regions of high error are restricted to low
209 temperatures above the bubble point line which has limited physical interest. It should further be
210 noted that this region also corresponds to conditions where solid formation may be expected, which
211 however is not accounted for in the current thermophysical model.

212 3.2. Shock tube tests

213 In order to assess the efficacy of the interpolation technique developed in this work as a means of
214 providing thermodynamic properties to flow simulations, two shock tube tests conducted are

215 simulated. For the first simulation, the states are chosen such that the fluid remains in the single-
216 phase region. For the second simulation the states are chosen to induce phase change in an initially
217 single-phase state. The conditions for the single and two-phase shock tube tests can be found in
218 Tables 3 and 4 respectively. In both cases, simulations are performed for both the binary and
219 quinternary mixtures using a CFL number of 0.2 and 200 computational cells.

220 3.2.1. Single phase

221 Figures 5 (a) to (c) show the profiles of the density, pressure and temperature respectively for both
222 the binary and quinternary mixture. As may be observed from Figure 5 (a) for the density of the
223 binary mixture, an expansion wave is observed at ca. 0.3 to 0.4 separating two constant states; this
224 is followed by a jump in the density across the discontinuity at ca. 0.6 before a smooth drop
225 beginning at ca 0.8 and ending at ca. 0.9. It is clear that the features of the results for the
226 quinternary mixture are the same as in the binary case, with the exception that they are at a lower
227 density level.

228 For the pressure (Figures 5 (b)) the results for both the binary and quinternary mixtures are almost
229 identical; as expected the discontinuity is still present. The slight variations are likely due to the
230 slight differences in the speed of sound and hence wave speeds. The temperature results show the
231 same similarities between the two mixtures (Figure 5 (c)). Importantly, the interpolated results
232 remain stable despite the presence of shock and rarefaction waves as well as contact discontinuities.

233 3.2.2. Two-phase

234 Figure 6 (a) to (d) shows the profiles of the density, vapour fraction, pressure and temperature
235 respectively, for the binary and quinternary mixtures. While the left hand states are the same and
236 the fluid is in the single-phase region, the state on the right is selected within the mixture's phase
237 envelope. Thus, relative to the dew line, the states are different for both of the two mixtures
238 simulated.

239 As Figure 6 (a) shows, for the binary mixture the density falls across the expansion wave which
240 begins at ca. 0.3 m and ends at ca. 0.4 m. The density drops sharply at 0.58 m, where the initial
241 boundary between the states was placed; this is followed by a slight distortion of the discontinuity at
242 ca. 0.62 m, representing an additional wave, and a slower drop across the shock between 0.64 m
243 and 0.68 m. Similar trends are observed for the quinternary mixture. However, the density
244 throughout is lower and the shock wave from 0.64 m is smeared over a larger distance.

245 The profiles of the vapour fraction (Figure 6 (b)) show that no vapour is produced across the
246 expansion wave. The vapour fraction is seen to increase through the series of waves between 0.58 m
247 and 0.64 m. Interestingly, across the shock wave, the vapour fraction increases for the binary and
248 decreases for the quinternary mixture, which is due to the different phase equilibria through the
249 respective mixture's phase envelopes.

250 Following the expansion wave, the pressures (Figure 6 (c)) obtained prior to the shockwaves is
251 substantially higher for the quinternary mixture, and in both cases relates to the bubble line
252 pressure of the fluids. In the case of the temperature (Figure 6 (d)), a fall is observed through the
253 expansion wave as with the density, after this however a sharp fall is seen at discontinuity before
254 rising and falling again. For this latter behaviour the quinternary mixture exhibits much larger
255 changes.

256 3.3. Decompression tests

257 In the following, the robustness of the HEM outflow model coupled with the interpolation technique
258 is evaluated for pipeline releases of CO₂ mixtures. The outflow model is validated against two sets of
259 experimental data obtained from Full-Bore Rupture (FBR) releases of CO₂ from a 144 m long, 150
260 mm internal diameter section of pipeline using the two mixtures introduced earlier (Cosham et al.,
261 2012). Table 1 presents the initial conditions and composition of fluid in the pipeline in both cases.
262 Given the very short depressurisation durations considered in both tests, heat transfer between the
263 pipe wall and the pipe surrounding is ignored in the model. The pipeline roughness was found
264 experimentally to be 0.005 mm, while the ambient pressure was 1.01 bara.

265 3.3.1. Binary mixture

266 Figure 7 shows comparison of the predicted and measured variation of the pressure at the closed
267 end of the section of pipeline following the initiation of the decompression. As may be observed in
268 the predicted results, the pressure remains initially constant but falls rapidly at ca. 0.2 s when the
269 initial expansion wave, caused by the decompression, reaches the closed end of the pipeline. The
270 experimental pressures shown were sampled with too low frequency to resolve this. Following this,
271 a pressure plateau of ca. 58 bara is predicted, until ca. 2.5 s at which point the pressure begins to fall
272 again towards the ambient. In comparison, after the initial pressure drop, the experimental pressure
273 is observed to fall more slowly to a minimum at ca. 1 s before recovering to a pressure very close to
274 the plateau pressure predicted by the model. This is practically important as this pressure is that
275 which is used in the analysis of the propagation of ductile fractures (Mahgerefteh et al., 2012a).
276 Following this the pressure again drops, but at a slower rate than that predicted. As noted by various
277 authors (Mahgerefteh et al., 2012b; Munkejord et al., 2010) this later behaviour is largely due to
278 frictional and heat transfer effects, the modelling of which is outside of this study.

279 Figure 8 shows the thermodynamic trajectory at the closed end of the pipeline section during the
280 decompression relative to the dew and bubble lines. As may be observed, as noted above, during
281 the initial decompression the fluid drops almost instantaneously along the isentrope into the phase
282 envelope where it descends towards the dew line at low temperatures.

283 3.3.2. Quinternary mixture

284 Figure 9 shows the comparison of the predicted pressures with the experimental data recorded at
285 transducers P14 and P18, 1.84 m and 3.64 m from the open end of the pipeline respectively
286 (Cosham et al., 2012). As may be observed, at both P14 and P18 the time at which the initial
287 pressure drop occurs, 2.75 and 5.5 ms respectively, is well captured. The recorded pressure during
288 the initial decompression is seen to be slower than that predicted; this deviation can partially be
289 explained by a lag in the measurements, given the rapidity in the pressure change.

290 Following this initial period of transients the simulations predict a steadying of the pressure at ca. 65
291 bara, at P18 this lasts for the duration of the simulation while for P14 the pressure begins to fall at
292 ca. 36 ms. In contrast, the measured data fall steadily throughout this period, this is likely in part due
293 to the effects of friction and heat transfer which the fluid model applied here does not capture
294 accurately (Mahgerefteh et al., 2012b). Notably the measured pressure at P14 indicates a
295 subsequent acceleration of the pressure drop at the time predicted by the fluid model.

296 4. Conclusions

297 This paper presents the development and application of a robust interpolation technique for the
298 prediction of thermodynamic properties and phase equilibria of complex mixtures. The accuracy and
299 computational burden of computing these physical properties greatly affects the overall accuracy
300 and computational cost of multiphase multicomponent simulations. Thus, the adaption of this
301 technique has a tremendous impact on our ability to perform sophisticated computational fluids
302 dynamics (CFD) simulations at reasonable cost without significant loss of accuracy.

303 The assessment of the technique's ability to reproduce the results of the EoS showed, for the most
304 part, an error no greater than 0.5 % compared to the actual EoS predictions. Large errors were
305 observed only for the liquid phase at low temperatures, where the physical model represented by
306 the EoS is itself not applicable, as solid formation not predicted by the EoS is expected. The
307 extension of the current interpolation technique to a thermophysical model where the solid phase is
308 accounted for is part of ongoing work.

309 Following this, the method was coupled with a fluid model and was used for the simulation of CO₂
310 rich mixtures, which is of particular interest in the development of CCS technology. Analysis of
311 several hypothetical shock tube tests, as well as the comparison of the predictions against
312 experimental decompression data, showed that the interpolation method produced robust and
313 highly reliable results for simple and complex mixtures.

314 Interestingly, comparison between model predictions and experimental decompression results
315 showed that the implementation of the interpolation technique produced a reasonable prediction of
316 the initial depressurisation period. On-going work by the authors focuses on the development of
317 appropriate models for the heat transfer and frictional effects to improve the accuracy of the
318 predictions beyond this period.

319 5. Acknowledgements

320 This work was supported by the UK Engineering and Physical Science Research Council (EPSRC
321 reference EP/K000446/1) and the European Union 7th Framework Programme FP7-ENERGY-2012-1-
322 2STAGE under grant agreement number 309102.

323 6. References

- 324 Akima, H., 1996. Algorithm 761: Scattered-data surface fitting that has the accuracy of a cubic
325 polynomial. *ACM Trans. Math. Softw.* 22, 365–371.
- 326 Andresen, T., 2009. Mathematical modeling of CO₂ based heat pumping systems. PhD Thesis. NTNU.
- 327 Blinkov, V., Jones, O., Nigmatulin, B., 1993. Nucleation and flashing in nozzles—2. Comparison with
328 experiments using a five-equation model for vapor void development. *Int. J. Multiph. Flow* 19,
329 965–986.
- 330 Brown, S., Fraga, E.S., Mahgerefteh, H., Martynov, S., 2015a. A geometrically based grid refinement
331 technique for multiphase flows. *Comput. Chem. Eng.* 82, 25–33.
332 doi:10.1016/j.compchemeng.2015.05.031
- 333 Brown, S., Martynov, S., Mahgerefteh, H., 2015b. Simulation of two-phase flow through ducts with
334 discontinuous cross-section. *Comput. Fluids* 120, 46–56. doi:10.1016/j.compfluid.2015.07.018
- 335 Castier, M., 2009. Solution of the isochoric–isoenergetic flash problem by direct entropy
DOI: 10.1016/j.compchemeng.2016.09.005

336 maximization. *Fluid Phase Equilib.* 276, 7–17. doi:10.1016/j.fluid.2008.10.005

337 Chen, N.H., 1979. An Explicit Equation for Friction Factor in Pipe. *Ind. Eng. Chem. Fundam.* 18, 296–
338 297. doi:10.1021/i160071a019

339 Cosham, A., Jones, D.G., Armstrong, K., Allason, D., Barnett, J., 2012. The Decompression Behaviour
340 of Carbon Dioxide in the Dense Phase, in: *Proceedings of the 2012 9th International Pipeline*
341 *Conference*. Asme, p. 447. doi:10.1115/IPC2012-90461

342 Diamantonis, N.I., Boulougouris, G.C., Mansoor, E., Tsangaris, D.M., Economou, I.G., 2013a.
343 Evaluation of Cubic, SAFT, and PC-SAFT Equations of State for the Vapor–Liquid Equilibrium
344 Modeling of CO₂ Mixtures with Other Gases. *Ind. Eng. Chem. Res.* 52, 3933–3942.
345 doi:10.1021/ie303248q

346 Diamantonis, N.I., Boulougouris, G.C., Tsangaris, D.M., Kadi, M.J. El, Saadawi, H., Negahban, S.,
347 Economou, I.G., 2013b. Thermodynamic and transport property models for carbon capture and
348 sequestration (CCS) processes with emphasis on CO₂ transport. *Chem. Eng. Res. Des.* 91, 1793–
349 1806. doi:10.1016/j.cherd.2013.06.017

350 Diamantonis, N.I., Economou, I.G., 2011. Evaluation of Statistical Associating Fluid Theory (SAFT) and
351 Perturbed Chain-SAFT Equations of State for the Calculation of Thermodynamic Derivative
352 Properties of Fluids Related to Carbon Capture and Sequestration. *Energy & Fuels* 25, 3334–
353 3343. doi:10.1021/ef200387p

354 Dumbser, M., Iben, U., Munz, C.D., 2013. Efficient implementation of high order unstructured WENO
355 schemes for cavitating flows. *Comput. Fluids* 86, 141–168.
356 doi:10.1016/j.compfluid.2013.07.011

357 Kontogeorgis, G.M., Folas, G.K., 2010. *Thermodynamic Models for Industrial Applications: From*
358 *Classical and Advanced Mixing Rules to Association Theories*. Wiley.

359 Leveque, R.J., 2002. *Finite Volume Methods for Hyperbolic Problems*. Cambridge University Press,
360 Cambridge.

361 Liou, M., 2006. A sequel to AUSM, Part II: AUSM+-up for all speeds. *J. Comput. Phys.* 214, 137–170.
362 doi:10.1016/j.jcp.2005.09.020

363 Mahgerefteh, H., Brown, S., Denton, G., 2012a. Modelling the impact of stream impurities on ductile
364 fractures in CO₂ pipelines. *Chem. Eng. Sci.* 74, 200–210. doi:10.1016/j.ces.2012.02.037

365 Mahgerefteh, H., Brown, S., Martynov, S., 2012b. A study of the effects of friction, heat transfer, and
366 stream impurities on the decompression behavior in CO₂ pipelines. ... *Gases Sci.* ... 379, 369–
367 379. doi:10.1002/ghg

368 Mahgerefteh, H., Oke, a, Rykov, Y., 2006. Efficient numerical solution for highly transient flows.
369 *Chem. Eng. Sci.* 61, 5049–5056. doi:10.1016/j.ces.2006.03.012

370 Martynov, S.B., Mason, D.J., Heikal, M.R., 2006. Numerical Simulation of Cavitation Flows Based on
371 Their Hydrodynamic Similarity. *Int. J. Engine Res.* 7, 283–296. doi:10.1243/14680874JER04105

372 Michelsen, M., 1982. The isothermal flash problem. Part II. Phase-split calculation. *Fluid Phase*
373 *Equilib.* 9, 21–40. doi:10.1016/0378-3812(82)85002-4

374 Michelsen, M.L., 1999. State function based flash specifications. *Fluid Phase Equilib.* 158-160, 617–
375 626. doi:10.1016/S0378-3812(99)00092-8

376 Michelsen, M.L., 1982. The isothermal flash problem. Part I. Stability. *Fluid Phase Equilib.* 9, 1–19.

377 Munkejord, S.T., Hammer, M., 2015. Depressurization of CO₂-rich mixtures in pipes: Two-phase flow
DOI: 10.1016/j.compchemeng.2016.09.005

- 378 modelling and comparison with experiments. *Int. J. Greenh. Gas Control* 37, 398–411.
379 doi:10.1016/j.ijggc.2015.03.029
- 380 Munkejord, S.T., Jakobsen, J.P., Austegard, A., MølInvik, M.J., 2010. Thermo- and fluid-dynamical
381 modelling of two-phase multi-component carbon dioxide mixtures. *Int. J. Greenh. Gas Control*
382 4, 589–596. doi:10.1016/j.ijggc.2010.02.003
- 383 Porter, R.T.J., Fairweather, M., Pourkashanian, M., Woolley, R.M., 2015. The range and level of
384 impurities in CO₂ streams from different carbon capture sources. *Int. J. Greenh. Gas Control* 36,
385 161–174. doi:10.1016/j.ijggc.2015.02.016
- 386 Saha, S., Carroll, J.J., 1997. The isoenergetic-isochoric flash. *Fluid Phase Equilib.* 138, 23–41.
387 doi:10.1016/S0378-3812(97)00151-9
- 388 Simões-Moreira, J., Bullard, C., 2003. Pressure drop and flashing mechanisms in refrigerant
389 expansion devices. *Int. J. Refrig.* 26, 840–848. doi:10.1016/S0140-7007(03)00070-7
- 390 Span, R., Wagner, W., 1996. A New Equation of State for Carbon Dioxide Covering the Fluid Region
391 from the Triple-Point Temperature to 1100 K at Pressures up to 800 MPa. *J. Phys. Chem. Ref.*
392 *Data* 25.
- 393 Zucrow, M.J., Hoffman, J.D., 1975. *Gas Dynamics*. Wiley, New York.
- 394

395

396

397 **Table 1. Initial conditions and fluid composition for decompression experiments Test 26 and 31**
 398 **(Cosham et al., 2012).**

Input Parameter	Test 26	Test 31
Feed Inlet Temperature (K)	278.35	283.15
Feed Inlet Pressure (bar)	141	151.51
Fluid Composition (% vol./vol)	N ₂ : 4.04 CO ₂ : 95.96	H ₂ : 1.15
		N ₂ : 4.0
		O ₂ : 1.87
		CH ₄ : 1.95 CO ₂ : 91.03

399

400 **Table 2. Average absolute deviations (%) of predictions of the temperature and pressure produced**
 401 **by the interpolation grids.**

Input Parameter	Binary	Quinternary
Temperature	0.005	0.002
Pressure	0.44	0.07

402

403

404 **Table 3. Initial states for the single-phase shock tube tests**

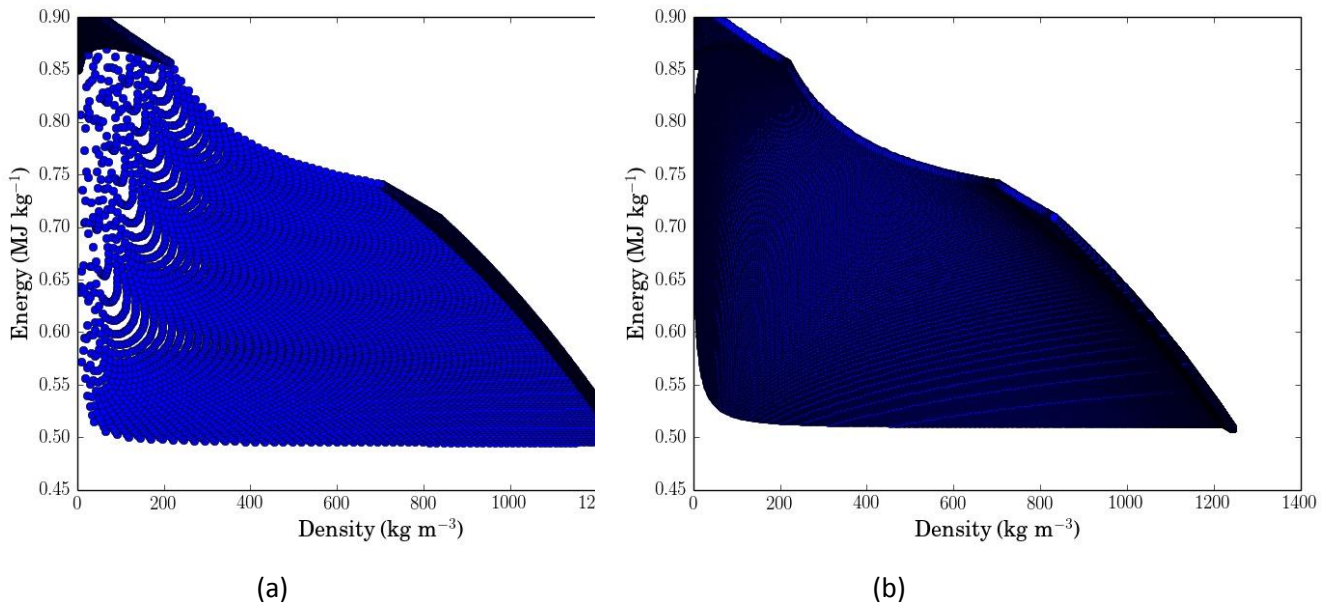
Input Parameter	P (bara)	Temperature (K)	Velocity (m s ⁻¹)
Left state	151	283.15	0
Right state	100	260.00	0

405

406 **Table 4. Initial states for the two-phase shock tube tests**

Input Parameter	P (bara)	Temperature (K)	Velocity (m s ⁻¹)
Left state	151	283.15	0
Right state	P _{dew} +2	260.00	0

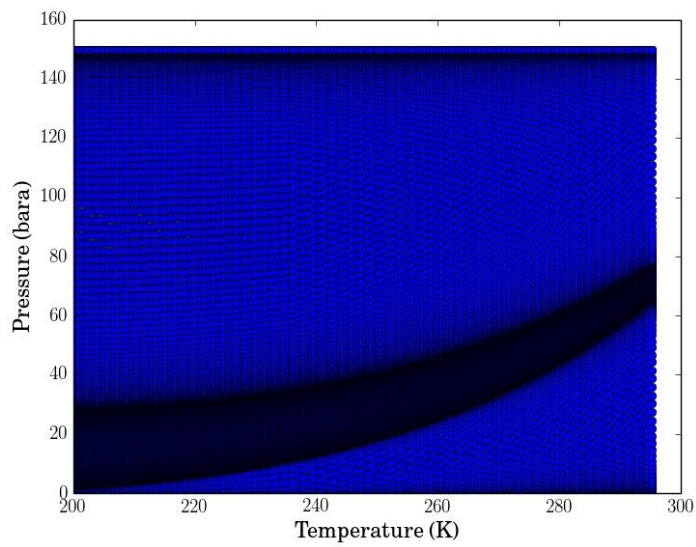
407



409

410 **Figure 1: The $\{\rho, e\}$ interpolation grids in the case of a uniform sampling (a) and with the adaptive**
 411 **sampling method (b) produced for the binary mixture of 95.96 % CO₂ - 4.04 % N₂ (vol/vol).**

412



413

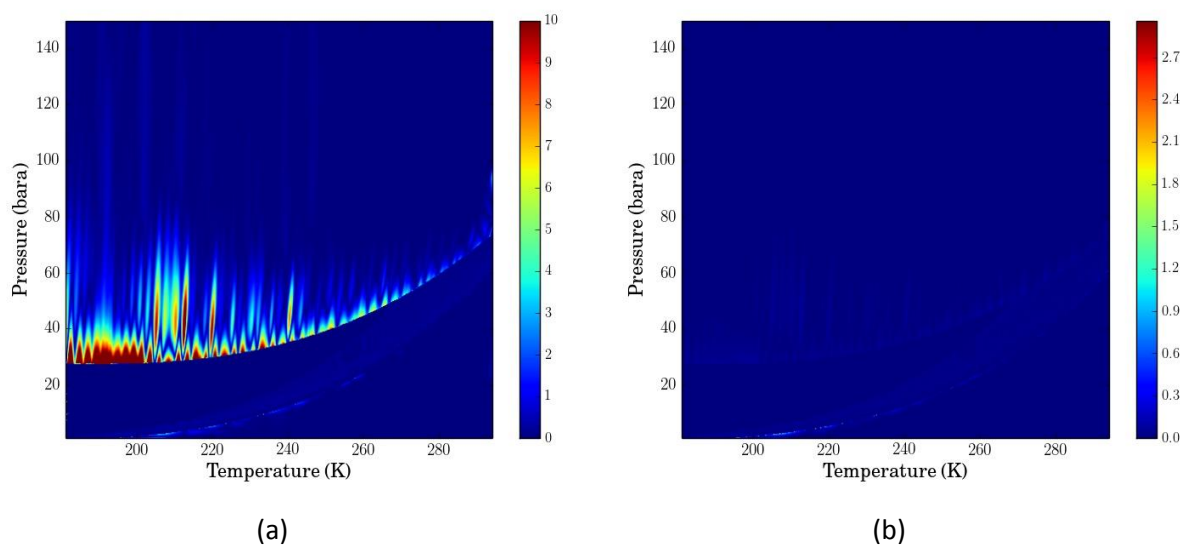
414 **Figure 2: The $\{P, T\}$ interpolation grid produced with the adaptive sampling method for the binary**
 415 **mixture of 95.96 %CO₂ - 4.04 % N₂ (vol/vol).**

416

417

418

419



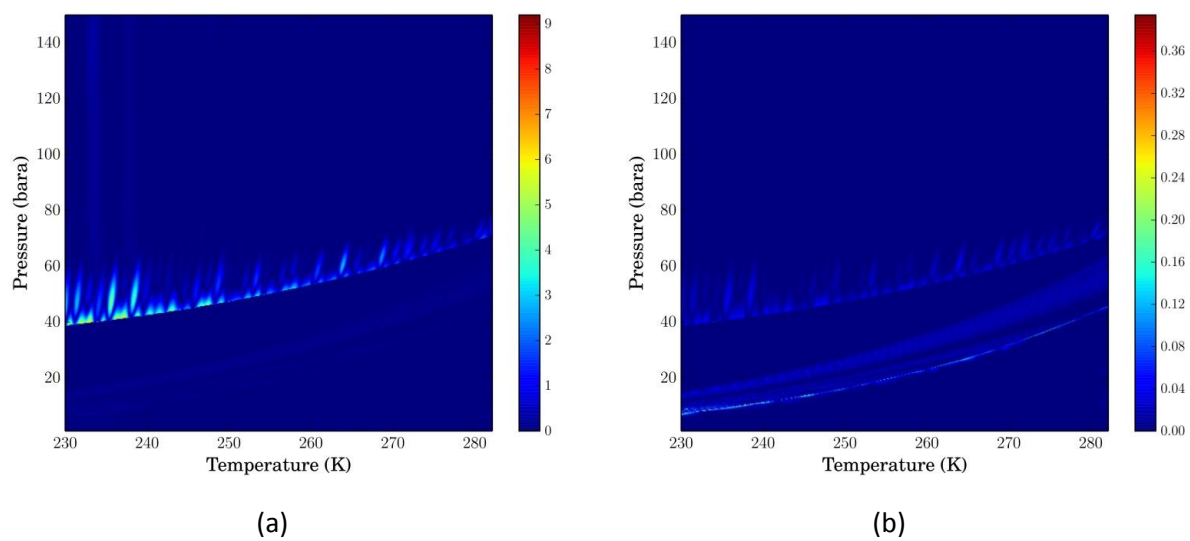
420

421 **Figure 3: %AAD interpolation errors observed in the pressure (a) and temperature (b) across the**
422 **relevant region in the P-T phase diagram for the binary mixture.**

423

424

425



426

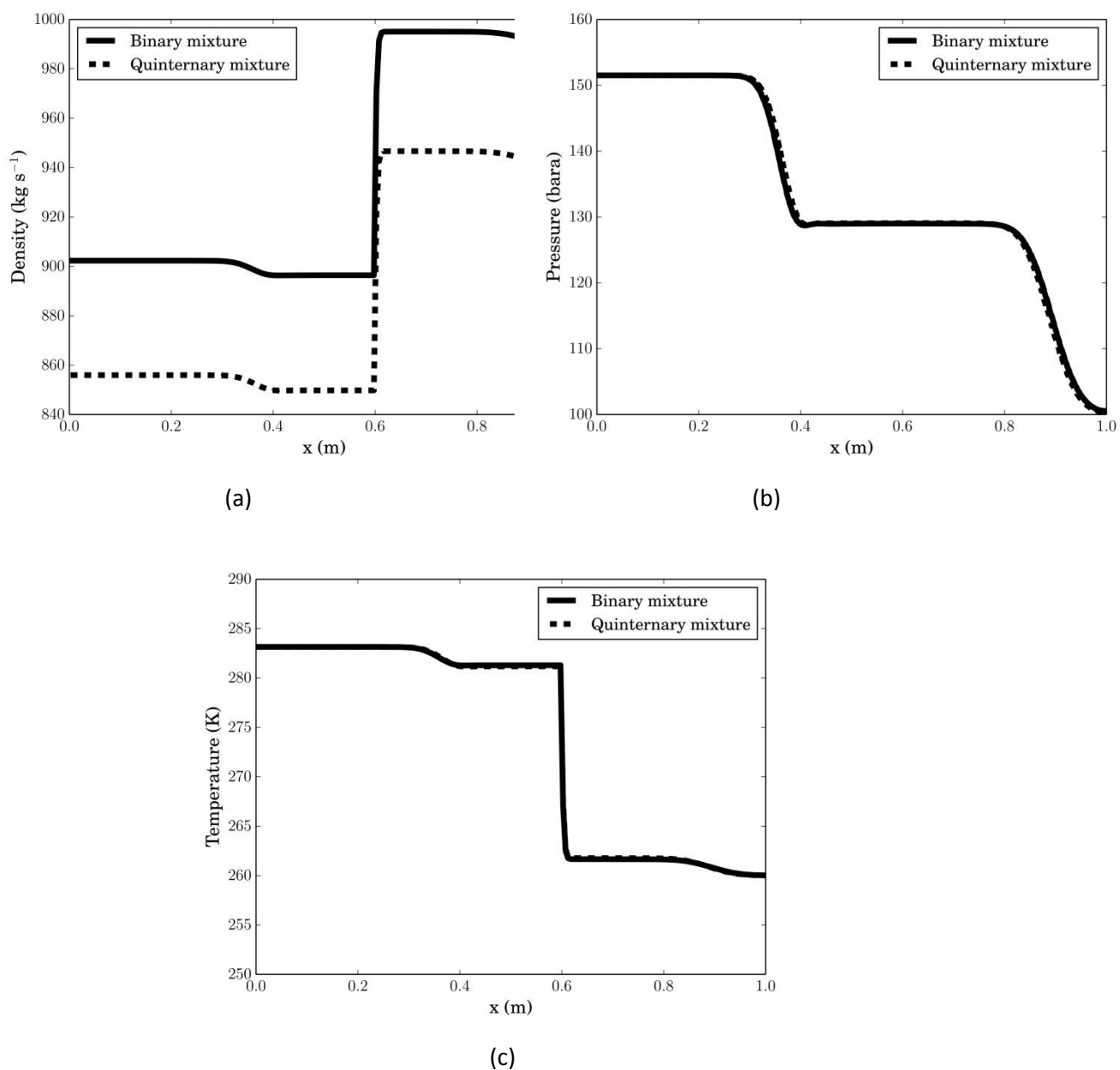
427 **Figure 4: %AAD interpolation errors observed in the pressure (a) and temperature (b) across the**
428 **relevant region in the P-T phase diagram for the quinary mixture.**

429

430

431

432

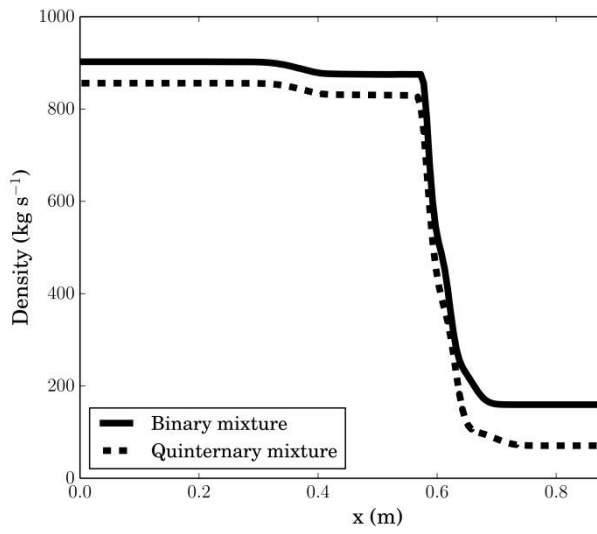


433 **Figure 5: Comparison of binary and quinternary mixture profiles of density (a), pressure (b) and**
434 **temperature (c) for the single-phase shock tube test after 0.4 ms.**

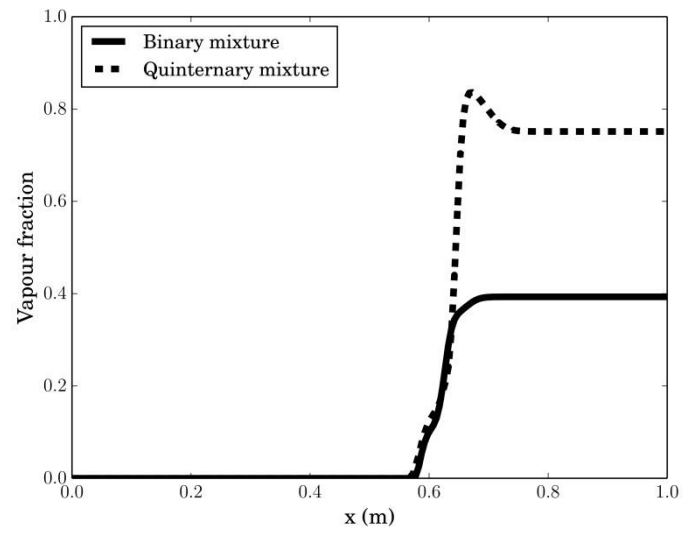
435

436

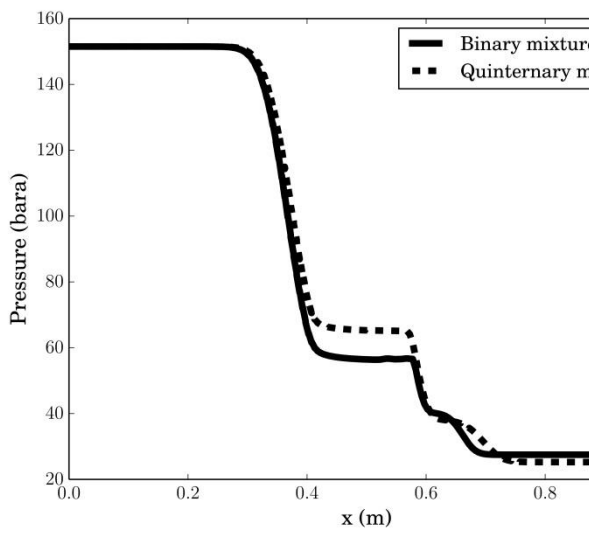
437



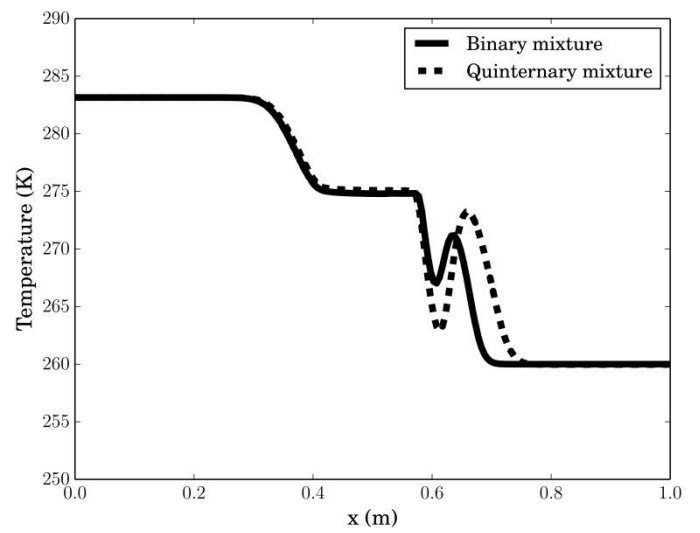
(a)



(b)



(c)

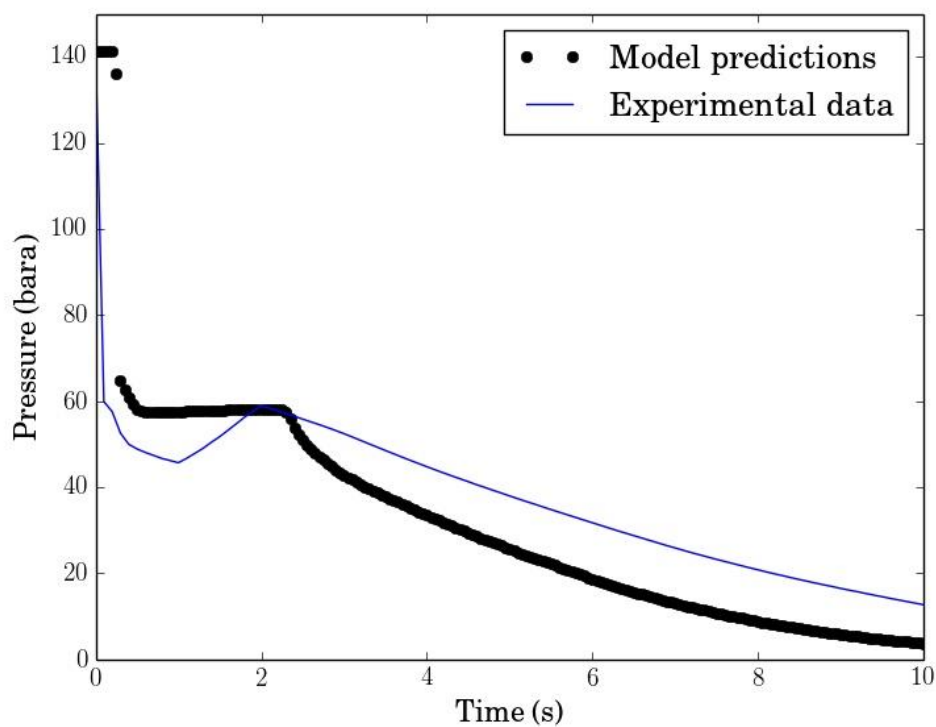


(d)

438

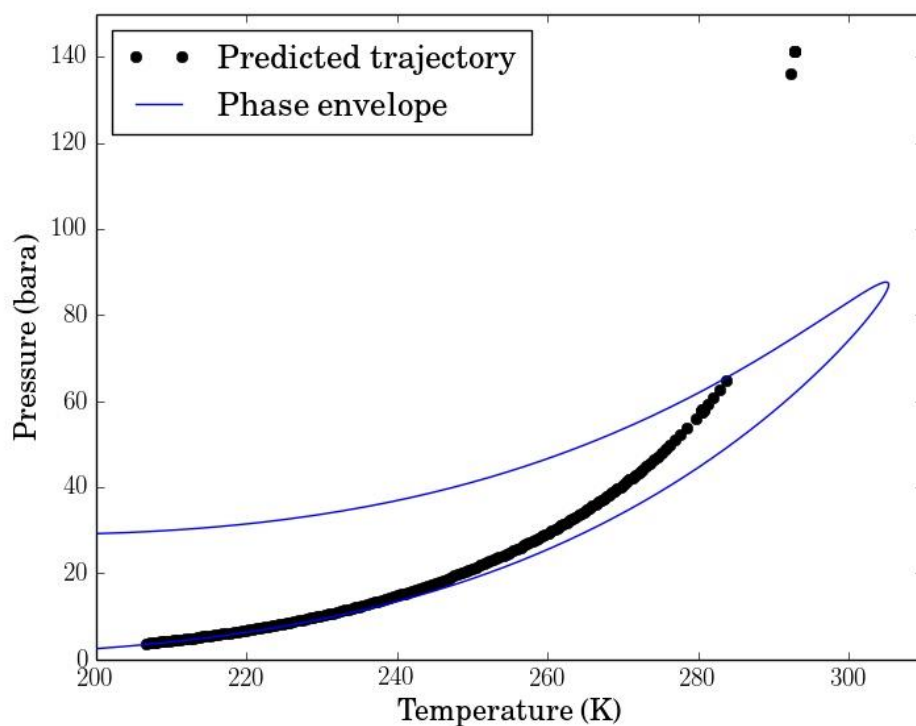
439 **Figure 6: Comparison of binary and quinternary mixture profiles of density (a), vapour fraction (b),**
440 **pressure (c) and temperature (d) for the two-phase shock tube test after 0.4 ms.**

441



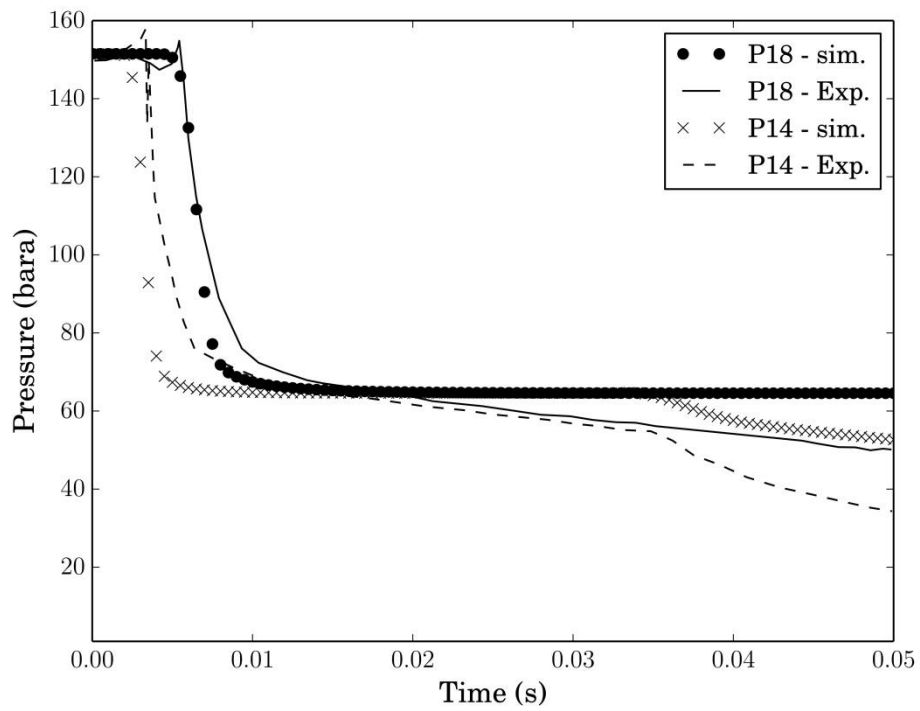
442

443 **Figure 7: Comparison of the predicted and measured variation of pressure with time at the closed**
 444 **end of the pipeline following the initiation of decompression.**



445

446 **Figure 8: Thermodynamic trajectory of the decompression relative to the binary mixture phase**
 447 **envelope at the closed end of the pipeline following the initiation of decompression.**



448

449 **Figure 9: Comparison of the predicted and measured variation of pressure with time 1.84 m (P14)**
 450 **and 3.84 (P18) from the open end of the pipeline following the initiation of decompression for the**
 451 **case of quinary mixture.**

452